Development of a Nonlinear Classical Polarization Model for Liquid Water and Aqueous Solutions: COS/D†

Anna-Pitschna E. Kunz and Wilfred F. van Gunsteren*

Laboratory of Physical Chemistry, Swiss Federal Institute of Technology ETH, 8093 Zürich, Switzerland

Received: April 6, 2009; Revised Manuscript Received: June 16, 2009

A new charge-on-spring (COS) model for water is introduced (COS/D). It includes a sublinear dependence of the induced dipole on the electric field for large field strength to include the effect of hyperpolarizability by damping the polarizability. Only two new parameters were introduced to define the damping of the polarizability. In the parametrization procedure, these two damping parameters, the two Lennard-Jones parameters, the charge on the oxygen, and the distance between the virtual site and the oxygen atom were varied to reproduce the density, the heat of vaporization, the dielectric permittivity, and the position of the first peak in the radial distribution function of liquid water at room temperature and pressure. In this way, a model was obtained that correctly describes a variety of thermodynamic, dynamic, and dielectric properties of water while still preserving the simplicity of the COS model, which allows a straightforward introduction of explicit polarization into (bio)molecular force fields.

1. Introduction

Faithful biomolecular simulation critically depends on the accuracy of the force field used. The most widely used general biomolecular force fields are all based on van der Waals and electrostatic nonbonded interaction terms using fixed (atomic) partial charges. Within this framework, polarization is only accounted for by structural rearrangement of (fragments of) molecules. Improved accuracy is to be reached by variation and optimization of the force field parameters. For example, the GROMOS (GROningen MOlecular Simulation) force field, based on reproducing the thermodynamic properties for small molecules, still improved its accuracy during the past decade. The newest parameter set 53A6 is able to reproduce the free energies of apolar (cyclohexane) and polar (water) solvation for typical biomolecular compounds.[1] However, a limitation of a nonpolarizable force field became eminent in this study. The attempt to simultaneously reproduce for polar compounds the free enthalpy of hydration and the density and heat of vaporization of the pure liquids by a combination of a (fixed) charge distribution and a set of van der Waals parameters failed for most functional groups considered.[1] This is not surprising as one expects the degree of (electronic) polarization of the solute to be larger when solvated in water compared to that in cyclohexane, which can only be achieved by using a polarizable molecular model or force field. Another example of the inadequacy of nonpolarizable force fields is the absence of the experimentally known maximum in the solvation free enthalpy of argon at intermediate composition of ethylene glycol and water mixtures using nonpolarizable models.[2] These and other findings reinforce the idea that a further improvement of biomolecular force fields should include polarizability.[3−9] There are several ways to introduce dipolar polarizability into classical simulations,[10,11] the point polarizable dipole model (PPD),[12−14] the charge-on-spring (COS)[15] (also called Drude oscillator[16] or shell)[17] model, and the fluctuating charge (FQ)[18] model. GROMOS polarizable force fields make use of the COS model[11] to integrate polarizability as it leads to simple formulas and is computationally efficient.

One additional deficiency of most polarizable models, apart from their larger demand for computing power than nonpolarizable ones, is their tendency to show overpolarization, leading to the polarization catastrophe and a static dielectric permittivity, $\varepsilon(0)$, that is too large.[19] There are several approaches to resolve these problems. The polarization catastrophe can be avoided by a big enough repulsive Lennard-Jones term[20] leading to dipole−dipole distances larger than $(4\alpha^2)^{1/6}$, by spreading the polarizability over more sites,[21] which lowers α and therefore the critical distance $(4\alpha^2)^{1/6}$, by introducing a distance-dependent damping factor for short-distance dipole−dipole interactions to keep them finite,[22] or by substituting the linear dependence of the induced dipole $\vec{\mu}_{\mathrm{ind}}$ on the electric field $\vec{E}$ for all values of $\vec{E}$ for a sublinear dependence for large field strengths,[11,23,24] which can be achieved by making the polarizability α electric-field-dependent. A remedy against a too large static dielectric permittivity $\varepsilon(0)$ is, for example, use of a polarizable site that is off of the charge site[25] or again a sublinear behavior for $\vec{\mu}_{\mathrm{ind}}$ for large field strengths. The method used in this paper, following an earlier described idea,[11,23] is the damping of the polarizability $\alpha_{\mathrm{D}} = \alpha_{\mathrm{D}}(E)$ for large $\vec{E}$ in an analytical way

$$\alpha_{\mathrm{D}} = \begin{cases} \alpha & \text{for } E \leq E_0 \\ \dfrac{\alpha E_0}{pE}\left[p + 1 - \left(\dfrac{E_0}{E}\right)^p\right] & \text{for } E > E_0 \end{cases} \quad (1)$$

where α is the original polarizability, E the value of the electric field $\vec{E}$, and p and E_0 are adjustable parameters of the model. The dependence of the induced dipole μ^{ind} on the electric field E ($\vec{\mu}^{\mathrm{ind}}$ along $\vec{E}$) with a damped polarizability α_D is displayed in Figure 1. The physical idea behind this approach of damping the polarizability α is to account for hyperpolarizability in a simplified scalar way as the linearity of $\vec{\mu}^{\mathrm{ind}} = \alpha\vec{E}$ is breaking down beyond some value of E. Nonlinear polarization effects begin to become significant at a field strength of 20−30

† Part of the "Walter Thiel Festschrift".

* To whom correspondence should be addressed. E-mail: wfvgn@igc.ethz.ch.

10.1021/jp903164s CCC: $40.75
Published on Web 08/10/2009

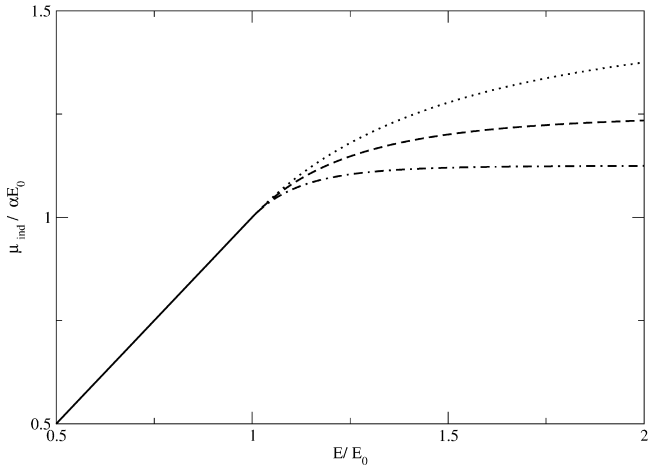

Figure 1. Dependence of the induced dipole μ_{ind} on the electric field strength **E** (eq 1). The solid line is the linear dependence up to E_0, the dotted line is the damped part for $p = 2$, the dashed is for $p = 4$, and the dash−dotted is for $p = 8$.

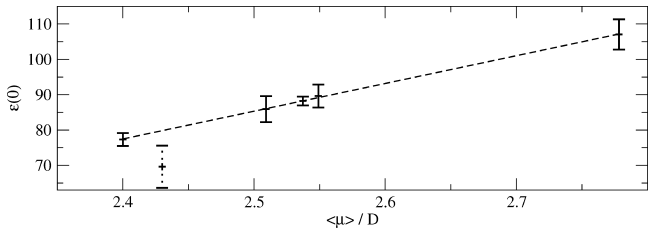

Figure 2. Relation between the static dielectric permittivity $\varepsilon(0)$ and the average molecular dipole moment $\langle\mu\rangle$ as observed in simulations of liquid water. The dotted line is a linear regression on the solid lined error bars, which were obtained from the parametrization (COS/D_A, COS/D_B, COS/D_C, COS/D_D, COS/D_E, COS/D_F) simulations. The error bar with the dashed line was obtained using the COS/D model.

V/nm$^{26-28}$ (about 150−250 (kJ mol^{-1} nm^{-3})$^{1/2}$) which is a strength that is comparable to the mean field strength in aqueous solution.[29,30] The chosen damping in Equation 1 can straightforwardly be included in biomolecular force fields where many-atom molecules are to be treated likewise.

Since our main interest is in simulating biological systems at physiological temperature and pressure and since biomolecules are generally solvated in water, our major goal was to develop a water model that reproduces the bulk liquid phase properties of water at room temperature and pressure as well as the nonpolarizable and previously developed polarizable models do. The gas phase properties of water, more representative for an isolated water molecule in a protein, are of less importance and the simulation of ice was merely done for completeness, as this phase is of little interest in biomolecular simulations.

The following properties were chosen for calibrating the parameters (p, E_0, q_O, d_{OM}, C_{12}, and C_6) of the model: the heat of vaporization ΔH_{vap}, the density ρ, the static dielectric permittivity $\varepsilon(0)$ estimated by the average molecular dipole $\langle\mu\rangle$ as predicted by Figure 2, and the position of the first peak in the oxygen−oxygen radial distribution function $g_{OO}(r)$, all at about 298 K and 1 atm. Using the optimized model parameters, other thermodynamic and dynamic properties and the solvation free energy of an argon probe were calculated to test the performance of the water model. To complete the study, the gas-phase dimer and the I_h ice were simulated.

2. Methods Section

2.1. Developing the Model. The damped model is based on previous COS models[11] in which the electric field $\vec{E}_i$, which influences the damping and the induced dipole, is taken at the position of the COS charge of the virtual site of atom i.[31] The dependence of the polarizability of the virtual site of atom i, α_i, on the electric field $\vec{E}_i$ at the COS of the virtual site of atom i, $\alpha_i = \alpha_i(|\vec{E}_i|)$, was chosen such that the induced dipole $\vec{\mu}_i^{ind}$ depends linearly upon the electric field $\vec{E}_i$ up to a certain field strength $E_{0,i}$ and then levels off to a constant value, as shown in Figure 1. Additionally, the function and its first derivative are to be continuous, which leads to the following formula for the induced dipole

$$\vec{\mu}_i^{ind} = \begin{cases} \alpha_i \vec{E}_i & \text{for } E_i \le E_{0,i} \\ \dfrac{\alpha_i E_{0,i}}{p_i}\left[p_i + 1 - \left(\dfrac{E_{0,i}}{E_i}\right)^{p_i}\right]\dfrac{\vec{E}_i}{E_i} & \text{for } E_i > E_{0,i} \end{cases} \quad (2)$$

where p_i is a parameter that determines the damping. This is like replacing the harmonic force constant k_i^{HO} of the spring by a harmonic force parameter $k_i^{HO}(E)$ that depends on the strength of the electric field $\vec{E}_i$ and becomes larger above the truncation parameter $E_{0,i}$. The self-polarization contribution to the potential energy, U_{self}, also becomes dependent on the electric field

$$U_{self,i} = \begin{cases} \dfrac{1}{2}\alpha_i \vec{E}_i^2 & \text{for } E_i \le E_{0,i} \\ \dfrac{1}{2}\alpha_i \vec{E}_{0,i}^2 + \dfrac{\alpha E_{0,i}^2}{p_i(p_i-1)}\left[-p_i^2 + (p_i^2-1)\left(\dfrac{E_i}{E_{0,i}}\right) + \left(\dfrac{E_{0,i}}{E_i}\right)^{p_i-1}\right] & \text{for } E_i > E_{0,i} \end{cases} \quad (3)$$

with $U_{self} = \sum_i U_{self,i}$, where i runs over all polarizable centers.

2.2. Simulation Methods. A cubic box with an edge length of 3.1057 nm was filled with 1000 water molecules, resulting in a density of 997 kg/m^3, corresponding to the density of liquid water at 298 K and 1 atm.[32] Molecular dynamics simulations were performed at constant pressure and temperature (NpT conditions) with the GROMOS96 package,[33,34] modified to incorporate the damped polarizable model. The geometry of the water molecules was constrained by applying the SHAKE algorithm[35] with a relative geometric tolerance of 10^{-4} on the OH bond length and on the intramolecular HH distance. The temperature was weakly coupled[36] to a bath of 298.15 K with a relaxation time of 0.1 ps, and the pressure was weakly coupled[36] to a bath of 1 atm with a relaxation time of 0.5 ps. The isothermal compressibility was set to the experimental value[32] of 7.513 × 10^{-4} (kJ mol^{-1} nm^{-3})$^{-1}$. The nonbonded van der Waals and electrostatic interactions were calculated using triple-range cutoff radii of 0.8/1.4 nm. The short-range interactions were calculated every time step by updating the molecular pair list for distances smaller than the first cutoff radius of 0.8 nm. For the intermediate range of distances between 0.8 and 1.4 nm, the pairlist was only updated every fifth time step, and at the same time, the interaction was calculated and kept unchanged between these updates. The long-range electrostatic interactions beyond the outer cutoff of 1.4 nm were represented by a reaction field[37,38] with $\varepsilon_{RF} = 78.5$. The equations of motion were integrated using the leapfrog algorithm with a time step of 2 fs. The velocities of the atoms at the beginning of the simulation were assigned from a Maxwell

distribution at 298 K. During the runs, configurations of the system were saved every 0.5 ps. The various properties for the COS/D water model were taken from a 2 ns simulation that followed a 50 ps equilibration period. To enhance convergence, the dielectric properties were calculated from 10 separate independent runs of 5 ns at 298.15 K. The starting structure of the ice I_h simulation was taken from the $3 \times 2 \times 2$ unit cell with 96 water molecules constructed by Hayward and Reimers[39] containing 12 copies of the smallest unit cell for ice I_h that contains 8 water molecules. To ensure a big enough box for the triple range cutoff, this $3 \times 2 \times 2$ unit cell was copied three times along each of the *x*-, *y*-, and *z*-axes. This box then had edges with sizes of 4.056, 4.684, and 4.416 nm. The structure was first equilibrated in five *NVT* simulations (each 5 ps long) with the temperature increasing from 1 to 50 K followed by three *NpT* runs (each 5 ps long) with the temperature increasing from 50 to 100 K. The simulation was performed at 100 K and 1 atm for 2 ns, and the configurations of the system were saved every 0.5 ps.

2.3. Parametrization. The model parameters were fit to reproduce the experimental density ρ and heat of vaporization ΔH_{vap} at room temperature and normal pressure. The heat of vaporization was calculated using the following formula

$$\Delta H_{\mathrm{vap}}(T) = -U_{\mathrm{liquid}}(T) + p\Delta V + Q^{\mathrm{int}} + Q^{\mathrm{ext}} = -U_{\mathrm{liquid}}(T) + RT + Q \quad (4)$$

where ΔH_{vap} is the experimental molar heat of vaporization, U_{liquid} is the computed intermolecular potential energy per mole, p the pressure, and ΔV the molar volume change between liquid and gas. R is the gas constant, and T is the absolute temperature. Q^{int} and Q^{ext} are quantum corrections. Q^{int} accounts for the difference in the vibrational energy between water in the liquid and the gas phases. Q^{ext} is a correction due to the intermolecular interaction in the liquid and is the difference in the vibrational energy calculated quantum mechanically and classically. At 298 K, this adds up to a total quantum correction[40] of $Q = -0.23$ kJ mol^{-1}.

Additionally, the average molecular dipole moment $\langle\mu\rangle$ (as an approximation for the very slowly converging dielectric permittivity $\varepsilon(0)$) and the first peak in the radial distribution function between the oxygens, g_{OO}, were chosen as reference points to be reproduced. The geometry was set to the experimental gas-phase values, and for α, the experimental polarizability of water was used, first only the electronic contribution and then including the vibrational contribution as the geometry of the water molecules was kept rigid.

The parameters that were varied were the charge $q_{\mathrm{O}} = -2q_{\mathrm{H}}$ (and accordingly the distance between the oxygen and the virtual site d_{OM} to keep the dipole at the experimental value), the attractive van der Waals parameter C_6, the repulsive van der Waals parameter C_{12} (both for the O−O interactions), the damping parameter p, and the truncation parameter E_0.

2.4. Analysis. ***2.4.1. Radial Distribution Function g(r).*** The structure of liquid water is characterized by a short-range order and a long-range disorder. This is reflected by the radial distribution function $g(r)$, which is experimentally available, for instance, through neutron diffraction.[41] The pair distribution function $g(r)$ gives the probability of finding another atom at a distance r from a given atom, relative to the probability expected for a completely uniform distribution at the same density, and can be calculated by a simple histogram summation in radial shells over all molecules in the system.

2.4.2. Self-Diffusion Coefficient D. The diffusion coefficient is obtained from the long-time limit of the mean square displacement according to the Einstein relation[42]

$$D = \lim_{t\to\infty} \frac{\langle(\vec{r}(t) - \vec{r}(0))^2\rangle}{6t} \quad (5)$$

where $\vec{r}(t)$ corresponds to the position vector of the center of mass at time t and the averaging is performed over both time and water molecules. In a similar way, we can calculate the *x*-, *y*-, and *z*- components of the diffusion constant D.

2.4.3. Rotational Correlation Times τ_l^α. Reorientational correlation functions, $C_l^\alpha(t)$, are calculated for three different axes α, the H−H vector, the O−H vector, and the molecular dipole vector $\vec{\mu}$, according to

$$C_l^\alpha(t) = \langle P_l(\vec{e}^{\,\alpha}(t)\cdot\vec{e}^{\,\alpha}(0))\rangle \quad (6)$$

where P_l is the Legendre polynomial of order l and $\vec{e}^{\,\alpha}$ is a unit vector pointing along the α-axis in a molecular reference frame. $C_l^\alpha(t)$ shows in general an exponential decay, which can, therefore, be fitted using the following expression

$$C_l^\alpha(t) = A\exp\left(-\frac{t}{\tau_l^\alpha}\right) \quad (7)$$

where τ_l^α denotes the single-molecule correlation time and A is a constant. The H−H and O−H relaxation can be obtained from ^{1}H $-^1$H and ^{17}O− ^{1}H dipolar relaxation NMR experiments, whereas the molecular dipolar orientational correlation function is experimentally obtained from optical measurements such as Raman scattering, fluorescence depolarization, or Kerr relaxation experiments.[43−45]

2.4.4. Dielectric Permittivity ε(0). The static dielectric constant or permittivity $\varepsilon(0)$ is calculated from the fluctuations in the total dipole of the simulation box according to a Kirkwood−Fröhlich-type equation derived by Neumann[46]

$$(\varepsilon(0) - 1)\left(\frac{2\varepsilon_{\mathrm{RF}} + 1}{2\varepsilon_{\mathrm{RF}} + \varepsilon(0)}\right) = \frac{\langle\vec{M}^2\rangle - \langle\vec{M}\rangle^2}{3\varepsilon_0 V k_{\mathrm{B}} T} \quad (8)$$

where $\varepsilon_{\mathrm{RF}}$ is the relative dielectric permittivity of the reaction field continuum that is used in the simulation, $\vec{M}$ is the total dipole moment of the system, V is the volume of the box, k_{B} is the Boltzmann constant, T is the absolute temperature, and ε_0 is the dielectric permittivity of vacuum.

2.4.5. Debye Relaxation Time τ_D and Frequency-Dependent Permittivity ε(ω). The Debye relaxation time τ_{D} can be obtained by calculation of the normalized autocorrelation function $\Phi(t)$ of the total dipole moment of the system

$$\Phi(t) = \frac{\langle\vec{M}(0)\vec{M}(t)\rangle}{\langle\vec{M}^2\rangle} \quad (9)$$

This function $\Phi(t)$ generally shows two decays, the first one being so fast that the used time resolution (a sampling rate of two per ps) is not able to capture it. It can, therefore, be approximated by a Heaviside function $\theta(t)$. The second decay is a single exponential decay. The $\Phi(t)$ function looks then as follows[47]

$$\Phi(t) = (1 - A)(1 - \theta(t)) + A\exp(-t/\tau_s) \quad (10)$$

The frequency-dependent dielectric permittivity $\varepsilon(\omega)$ of the system can be obtained from the normalized autocorrelation function $\Phi(t)$ of the total dipole moment $\vec{M}$ of the system, using its Fourier−Laplace transform[48]

$$\frac{(\varepsilon(\omega) - 1)}{(\varepsilon(0) - 1)}\frac{(2\varepsilon_{RF} + \varepsilon(0))}{(2\varepsilon_{RF} + \varepsilon(\omega))} = \int_0^\infty \left(-\frac{d\Phi}{dt}\right)\exp(-i\omega t)dt \quad (11)$$

Assuming Debye dielectric behavior after the first initial phase, one has[47−50]

$$\frac{\varepsilon(\omega) - \varepsilon(\infty)}{\varepsilon(0) - \varepsilon(\infty)} = \frac{1}{1 + i\omega\tau_D} \quad (12)$$

Inserting eq 10 into eq 11 and using eq 12, one finds the infinite-frequency dielectric permittivity $\varepsilon(\infty)$

$$\varepsilon(\infty) = 1 + \frac{(1 - A)(\varepsilon(0) - 1)}{1 + A\lambda} \quad (13)$$

and the Debye relaxation time τ_D

$$\tau_D = (1 + A\lambda)\tau_s \quad (14)$$

with

$$\lambda = \frac{\varepsilon(0) - 1}{2\varepsilon_{RF} + 1} \quad (15)$$

2.4.6. Finite and Infinite System Kirkwood Factors G_k and g_k. The finite system Kirkwood factor G_k measures the orientational correlation between a single dipole and all of its peers. It is determined from

$$G_k = \frac{\langle M^2\rangle - \langle M\rangle^2}{N\langle\mu^2\rangle} \quad (16)$$

where N is the number of molecules and μ is the dipole moment of a single molecule. The finite system Kirkwood factor G_k depends on the boundary conditions (ε_{RF}) and the box shape. For our simulation conditions, the relation to the infinite system Kirkwood factor g_k,[49] which is available experimentally, is

$$g_k = \frac{(2\varepsilon_{RF} + \varepsilon(0))(2\varepsilon(0) + 1)}{3\varepsilon(0)(2\varepsilon_{RF} + 1)}G_k \quad (17)$$

2.4.7. Heat Capacity C_p. The heat capacity at constant pressure can be approximated[40] according to the formula

$$C_p \approx \frac{U_2^{tot} - U_1^{tot}}{T_2 - T_1} + \frac{\partial Q^{int}}{\partial T} + \frac{\partial Q^{ext}}{\partial T} \quad (18)$$

where U^{tot} is the total energy per molecule and Q^{int} is the quantum contribution of the intramolecular vibrational modes to the specific heat, while Q^{ext} is the difference between the quantum mechanical and classical intermolecular vibrational energy. These quantum contributions add up to about −9.3 J mol^{-1} K^{-1} at 298 K and 1 atm.

TABLE 1: Effects of the COS/D Model Parameters on the Properties of Liquid Water[a]

	ρ	ΔH_{vap}	R_{max}	$\langle\mu\rangle$
increasing q_H	↑	↑↑	∼	↑
increasing α	↑	↑	∼	↑
increasing C_{12}	↓	↓↓	↑	∼
increasing C_6	↑	↑	↓↓	∼
increasing p	↓	↓	∼	↓
increasing E_0	↑	↑	∼	↑

[a] Symbols and variables: One arrow: dependence visible; two arrows: stronger dependence; tilda: neglegable dependence; q_H: charge of the H atom; α: molecular polarizability; C_{12}: repulsive oxygen−oxygen Lennard-Jones parameter; C_6: attractive oxygen−oxygen Lennard-Jones parameter; p: damping parameter; E_0: truncation parameter; ρ: density; ΔH_{vap}: heat of vaporization; R_{max}: first peak in the oxygen−oxygen radial distribution function; $\langle\mu\rangle$: averaged molecular dipole moment.

For this purpose, we carried out three additional *NpT* simulations of 1 ns each (plus an initial 100 ps of equilibration) at 298, 318, and 338 K.

2.4.8. Thermal Expansion Coefficient α. The thermal expansion coefficient α is calculated using a finite-difference expression[51]

$$\alpha = \frac{1}{V}\left(\frac{\partial V}{\partial T}\right)_p \approx -\left(\frac{\ln(\rho_2/\rho_1)}{T_2 - T_1}\right)_p \quad (19)$$

2.4.9. Isothermal Compressibility κ_T. The isothermal compressibility κ_T can be obtained by the following finite-difference expression[52]

$$\kappa_T = -\frac{1}{V}\left(\frac{\partial V}{\partial p}\right)_T = \frac{1}{\rho}\left(\frac{\partial \rho}{\partial p}\right)_T = \left(\frac{\partial \ln(\rho)}{\partial p}\right)_T \approx \left(\frac{\ln(\rho_2/\rho_1)}{p_2 - p_1}\right)_T \quad (20)$$

where ρ is the density of the system. For this purpose, we carried out three additional *NVT* simulations of 1 ns each (plus an initial 100 ps of equilibration) at densities of 947.0, 997.0, and 1047.0 kg m^{-3}.

2.4.10. Surface Tension γ. The surface tension can be calculated using the following expression

$$\gamma = \frac{L_z}{2}\left\langle\left(p_{zz} - \frac{1}{2}(p_{xx} + p_{yy})\right)\right\rangle \quad (21)$$

where L_z is the length of the box in the z direction, $\langle ...\rangle$ denotes a time averaging, and p_{ii} are the diagonal elements of the pressure tensor. To calculate the surface tension, an additional 1 ns simulation was performed with a box of 1000 particles, where the box length in the z direction was extended to 15 nm.

2.4.11. Free Enthalpy of Solvation ΔG_S. The free enthalpy of solvation ΔG_S of argon as a case of a hydrophobic probe can be determined via Widom test particle insertion[53] of an argon probe with van der Waals parameters $C_6 = 6.2647225$ kJ mol^{-1} nm^6 and $C_{12} = 9.847044$ kJ mol^{-1} nm^{12} and a polarizability[54] $(1/4\pi\varepsilon_0)\alpha$ of 1.586×10^{-3} nm^3. For 600 water configurations of the simulation, 2.1×10^5 test insertions were performed.

From the volume- and Boltzmann-weighted average of the interaction energy U_{int} between the argon probe and the solvent molecules, ΔG_S was calculated from[53,55]

$$\Delta G_S = -k_B T \ln\left(\frac{\langle V \exp(-U_{int}/k_B T)\rangle}{\langle V\rangle}\right) \tag{22}$$

where V is the volume of the box. U_{int} contains two terms[2] in case of a polarizable argon probe. One is the van der Waals term, and the other one is the induced dipolar interaction energy U_{dip}

$$U_{dip} = -\frac{1}{2}\alpha E^2 \tag{23}$$

for simplicity taken from linear response theory (without damping), where E is the size of the electric field at the argon probe due to all other partial charges (including charges-on-spring).

Argon solvation solute−solvent (uv) interaction enthalpies ΔH_{uv} and entropies $T\Delta S_{uv}$ were determined via

$$\Delta H_{uv} = \frac{\langle U_{int} V \exp(-U_{int}/k_B T)\rangle}{\langle V \exp(-U_{int}/k_B T)\rangle} \tag{24}$$

and

$$T\Delta S_{uv} = \Delta H_{uv} - \Delta G_S \tag{25}$$

Note that ΔH_{uv} and $T\Delta S_{uv}$ are not directly available from experiment. Because there are no solute−solute interactions in a single argon probe and the solvent−solvent interaction enthalpy and entropy cancel exactly,[55,56] the solute−solvent terms are the ones that determine the driving force of the solvation.[2,55]

3. Results

3.1. Liquid Phase. ***3.1.1. Variation of Model Parameters.*** The impact of changing a single force field parameter on the properties of the water model derived from observations made during the parametrization process are summarized in Table 1, the details are given in Tables 2 and 3, and the final COS/D model parameters are presented in Table 4. These properties are the heat of vaporization (ΔH_{vap}), the density (ρ), the position of the first maximum in the oxygen−oxygen radial distribution function (R_{max}), and the average molecular dipole moment ($\langle\mu\rangle$).

A first approach starting from the COS/B2 model (Table 4), where the charge on the spring is attached to the oxygen, did not lead to satisfying results for COS/DB type of models (Table 2). Fitting both the density ρ and the heat of vaporization ΔH_{vap} to the experimental values while keeping the radial distribution function $g(r)$ and the dielectric permittivity $\varepsilon(0)$ close to the experimental values turned out to be impossible for the COS/DB type of model. A fraction of the results of the parametrization are shown in Table 2 to illustrate this.

Next, the COS/G2 model (Table 4), which has its charge-on-spring attached to a virtual site M at a distance d_{OM} from the oxygen on the molecular symmetry axis on the side of the H atoms, was used as a starting point. For this COS/D type of model, a satisfactory parameter set could be found (Table 3).

TABLE 2: Collection of Parameter Sets and the Influence of Their Variation on Certain Properties for the Model with the Charge on the Spring at the Oxygen[a]

	μ_0 [D]	$\alpha(4\pi\varepsilon_0)^{-1}$ [10^{-3} nm^3]	C_{12} [10^{-6} kJ mol^{-1} nm^{12}]	C_6 [10^{-3} kJ mol$^-$ nm^6]	p	E_0 [kJ mol^{-1} nm^{-3}]$^{1/2}$	ρ [kg m^{-3}]	ΔH_{vap} [kJ mol^{-1}]	U_{pol}/ [kJ mol^{-1}]	U_{LJ} [kJ mol^{-1}]	U_{cmb} [kJ mol^{-1}]	R_{max} [nm]	$\langle\mu\rangle$ [D]
COS/DB$_1$	1.9	1.4	2.57	2.91	2	150	1027	40.1	24.4	14.3	−76.5	0.271	2.844
COS/DB$_2$	1.95	1.4	2.57	2.91	2	150	1052	42.6	28.1	16.6	−85.2	0.271	2.938
COS/DB$_3$	1.95	1.5	2.57	2.91	2	150	1081	43.1	34.6	19.0	−94.6	0.269	3.050
COS/DB$_4$	1.95	1.2	2.52	2.86	4	125	972	36.6	15.7	10.4	−60.5	0.275	2.604
COS/DB$_5$	1.95	1.2	2.62	2.86	4	125	985	37.2	16.0	10.2	−61.3	0.275	2.609
COS/DB$_6$	1.95	1.2	2.62	2.91	4	125	978	37.0	15.4	10.0	−60.2	0.273	2.603
COS/DB$_7$	1.95	1.15	2.8	2.85	2	125	1015	39.0	16.0	9.8	−62.6	0.273	2.611
COS/DB$_8$	1.95	1.15	2.8	2.85	2	130	1022	39.8	16.0	10.0	−63.7	0.273	2.628
COS/DB$_9$	1.95	1.15	2.8	2.85	3	125	1015	38.7	15.2	9.4	−61.2	0.273	2.592

[a] Variables: μ_0: fixed molecular dipole moment; α: molecular static polarizability; C_{12}: repulsive oxygen−oxygen Lennard-Jones; C_6: attractive oxygen−oxygen Lennard-Jones coefficient; p: damping parameter; E_0: truncation parameter; ρ: density; ΔH_{vap}: heat of vaporization; U_{pol}: polarization energy; U_{LJ}: Lennard-Jones energy; U_{cmb}: Coulomb energy; R_{max}: position of the first peak in the oxygen−oxygen radial distribution function; $\langle\mu\rangle$: averaged molecular dipole moment; $\varepsilon(0)$: dielectric permittivity.

TABLE 3: Collection of Parameter Sets and the Influence of Their Variation on Certain Properties for the Model with the Charge on the Spring at a Virtual Site M[a]

	q_H [D]	$\alpha(4\pi\varepsilon_0)^{-1}$ [10^{-3} nm^3]	C_{12} [10^{-6} kJ mol^{-1} nm^{12}]	C_6 [10^{-3} kJ mol^{-1} nm^6]	p	E_0 [kJ mol^{-1} nm^{-3}]$^{1/2}$	ρ [kg m^{-3}]	ΔH_{vap} [kJ mol^{-1}]	U_{pol}/ [kJ mol^{-1}]	U_{LJ} [kJ mol^{-1}]	U_{cmb} [kJ mol^{-1}]	R_{max} [nm]	$\langle\mu\rangle$ [D]	$\varepsilon(0)$
COS/D	0.5863	1.4945	3.25	3.45	8	99	997	43.9	16.5	12.7	−71.0	0.275	2.482	69.8
COS/D$_1$	0.58	1.4945	3.1	3.35	8	99	991	43.3	16.6	13.0	−70.6	0.275	2.483	
COS/D$_2$	0.6055	1.4945	3.1	3.35	8	99	1000	46.1	17.4	15.0	−76.3	0.273	2.482	
COS/D$_3$	0.58	1.4945	3.3	3.35	8	99	1018	44.4	16.9	12.4	−71.5	0.273	2.483	
COS/D$_4$	0.58	1.4945	3.1	3.45	8	99	976	42.5	16.1	12.8	−69.2	0.277	2.482	
COS/D$_5$	0.6055	1.4945	3.24	3.46	4	100	1072	49.2	20.2	14.3	−82.0	0.273	2.539	
COS/D$_6$	0.6055	1.4945	3.24	3.46	4	200	1152	60.3	41.2	25.8	−125.0	0.275	3.055	
COS/D$_A$	0.5265	1.494	3.24	3.46	8	100	978	43.8	9.1	8.9	−59.6	0.275	2.400	77.3
COS/D$_B$	0.5265	1.494	3.24	3.46	8	110	987	44.9	10.8	9.9	−63.4	0.273	2.509	85.9
COS/D$_C$	0.5265	1.494	3.24	3.46	2	100	988	45.4	12.2	10.6	−66.0	0.275	2.537	88.2
COS/D$_D$	0.5265	1.494	3.24	3.46	8	1000	1021	47.4	21.5	14.4	−81.1	0.275	2.778	107.1

[a] Variables: q_H: point charge on the hydrogen; α: molecular static polarizability; C_{12}: repulsive oxygen−oxygen Lennard-Jones; C_6: attractive oxygen−oxygen Lennard-Jones coefficient; p: damping parameter; E_0: truncation parameter; ρ: density; ΔH_{vap}: heat of vaporization; U_{pol}: polarization energy; U_{LJ}: Lennard-Jones energy; U_{cmb}: Coulomb energy; R_{max}: position of the first peak in the oxygen−oxygen radial distribution function; $\langle\mu\rangle$: averaged molecular dipole moment; $\varepsilon(0)$: dielectric permittivity.

The density is increased when increasing the charge of the hydrogen atoms while also increasing the distance between the virtual site and the oxygen to keep the permanent dipole constant, the polarizability, or the truncation parameter or when decreasing the damping parameter as all of this increases the Coulombic interaction, leading to a denser packing. Obviously, the density will increase upon increasing the attractive van der Waals parameter or decreasing the repulsive oxygen−oxygen van der Waals parameter.

The heat of vaporization shows a qualitatively similar dependence on an increase or decrease of the parameters as the density but a bit stronger one on a change of the charge on the hydrogen atoms and on increasing the repulsive oxygen−oxygen van der Waals parameter. An increase of the van der Waals well depth ($\varepsilon_{LJ} = C_6^2/(4C_{12})$) leads to a decrease of the heat of vaporization, which is due to the fact that the Lennard-Jones potential energy is positive for liquid water. This complicates the parametrization.

The position of the first peak in the oxygen−oxygen radial distribution is only dependent on the oxygen−oxygen van der Waals parameters, proportional to the repulsive one and a bit stronger than the reverse proportional to the attractive one. The latter shows a stronger effect.

The average molecular dipole is not sensitive to the oxygen−oxygen van der Waals parameter. As expected, it responds with increasing upon increasing the polarizability or the truncation parameter or upon decreasing the damping parameter.

The observed dependencies indicate that by varying these six parameters, the experimental values of the four observables should be reproducible.

The final parameters that we chose for the COS/D model are given in Table 4 together with those of a few previous water models to which the COS/D model is compared in the next subsection.

3.1.2. Comparison of the COS/D Model with Other Models. The nonpolarizable models SPC[57] and SPC/E[58] and the polarizable models COS/B2[20] and COS/G2[25] were selected for comparison to the COS/D model because a wide range of liquid state properties are available for these models.[20,25,59] For a comparison of such properties for yet other water models, we refer to refs 60−64.

Thermodynamic Properties. In Table 5 the energetic properties and the densities of the SPC, SPC/E, COS/B2, COS/G2, and COS/D models are given. The density ρ of the SPC model is known to be too low. The densities of the polarizable models COS/B2, COS/G2, and COS/D and the SPC/E model are in better agreement with experiment. The heat of vaporization ΔH_{vap} is in accordance with experiment for all models except SPC/E, which has a larger value because of the additionally integrated polarization energy.[58]

The main contribution to the potential energy U_{pot} is the Coulombic energy U_{cmb}. The contribution from the Lennard-Jones energy U_{LJ} is 17−25%. For the polarizable models, the polarization energy U_{self} is between a fourth and a third of the potential energy U_{pot}.

The surface tension γ shows too low values for SPC and SPC/E water, a tendency that is also observable with other water models.[65] The COS/D model has a surface tension close to the experimental value.

The heat capacity C_p and the thermal expansion coefficient α are shown for three different models in Table 6. The heat capacity C_p is reasonably well reproduced by all models. The coefficients of thermal expansion α are overestimated by the

TABLE 4: Parameters of Three COS Polarizable Water Models and the SPC and SPC/E Models for Comparison[a]

model	exp	SPC[57]	SPC/E[58]	COS/B2[20]	COS/G2[25]	COS/D
number of force sites		3	3	4	5	5
d_{OH}/[nm]	0.0957(3)(gas),[70] 0.0970(5)(liq)[71]	0.1	0.1	0.1	0.09572	0.09572
∠HOH/[deg]	104.52(5)(gas),[70] 106.1(18)(liq)[71]	109.47	109.47	109.47	104.52	104.52
d_{OM}/[nm]					0.022	0.0257
p						8
E_0/[kJ mol^{-1} nm^{-3}]$^{1/2}$						99
q_H/[e]		0.41	0.4238	0.373	0.5265	0.5863
q_O/[e]		−0.82	−0.8476	−0.746	0	0
q_M/[e]					−1.0530	−1.1726
μ^0/[D]	1.855[72]	2.27	2.35	2.07	1.85	1.855
q_{pol}/[e]				−8.0	−8.0	−8.0
$\alpha(4\pi\varepsilon_0)^{-1}$/[10^{-3} nm^3]	1.494(7)			0.930	1.255	1.4945
C_6/[10^{-3} kJ mol^{-1} nm^6]		2.61735	2.61735	2.75691	3.24434	3.25
C_{12}/[10^{-6} kJ mol^{-1} nm^{12}]		2.63413	2.63413	3.01500	3.45765	3.45

[a] Variables: d_{OH}: OH bond length; ∠HOH: HOH bond angle; d_{OM}: oxygen−virtual M site distance; p: damping parameter; E_0: truncation parameter; q_H: partial charge on the hydrogen; q_O: partial charge on the oxygen; q_M: partial charge on the virtual M site; μ^0: fixed molecular dipole moment; q_{pol}: COS polarisation charge; α: molecular polarizability (which is the mean electronic polarizability $(1.457(3)(4\pi\varepsilon_0)^{-1} \times 10^{-3}$ nm^3)[73] plus the vibrational contribution $(0.037(4\pi\varepsilon_0)^{-1} \times 10^{-3}$ nm^3)[74] in the low-frequency limit); C_6: attractive Lennard-Jones coefficient; C_{12}: repulsive Lennard-Jones coefficient, both for oxygen−oxygen interactions.

TABLE 5: Liquid State Properties of Different Water Models at 1 atm and 298.15 K (for expt, SPC, SPC/E, COS/D) and 300 K (for COS/B2, COS/G2)[a]

model	expt	SPC[20,59,65]	SPC/E[59,65]	COS/B2[20,75]	COS/G2[25]	COS/D
T/[K]	298.15	300.7	301.0	302.5	302.8	296.8
p/[atm]	1			5.5	0.93	0.8
ρ/[kgm^{-3}]	997[32]	972	994	992	997	997
ΔH_{vap}/[kJ mol^{-1}]	44.05[19]	43.7	48.8	44.2		44.0
γ/[mN m^{-1}]	71.6[65]	53.4	61.3			72.9
U_{pot}/[kJ mol^{-1}]	−41.5[40]	−41.3		−41.7	−41.3	−41.8
U_{cmb}/[kJ mol^{-1}]		−48.2		−64.0		−70.9
U_{self}/[kJ mol^{-1}]		−		11.5	15.4	16.5
U_{LJ}/[kJ mol^{-1}]		7.0		10.7		12.7

[a] Variables: T: temperature; p: pressure; ρ: density; ΔH_{vap}: heat of vaporization; γ: surface tension; U_{pot}: total potential energy; U_{cmb}: Coulomb energy; U_{self}: self-polarization energy; U_{LJ}: Lennard-Jones energy.

TABLE 6: Heat Capacity C_p and Thermal Expansion Coefficient α at 1 atm Pressure[a]

T/[K]	U^{tot}/[kJ mol^{-1}]	C_p/[J mol^{-1} K^{-1}]	ρ/[kg m^{-3}]	α/[10^{-4} K]
		Exp		
298		75.32[76]	997[32]	2.57[32]
318		75.31[76]	990[32]	4.22[32]
338		75.43[76]	980[32]	5.54[32]
		SPC[20]		
298	−33.72		972	
		74.2		8.13
318	−32.25		956	
		73.7		9.99
338	−30.59		937	
		COS/B2[20]		
298	−34.65		997	
		86.7		10.1
318	−32.73		977	
		85.2		11.0
338	−30.84		956	
		COS/D		
298	−34.40		997	
		62.2		1.3
318	−32.97		994	
		62.2		3.5
338	−31.54		987	

[a] Variables: T: temperature; U^{tot}: total energy; ρ: density.

TABLE 7: Isothermal Compressibility κ_T of Different Water Models at 298 K[a]

ρ/[kg m^{-3}]	p/[atm]	κ_T/[10^{-6} atm^{-1}]
	Exp	
997	1	45.8[32]
	SPC[20]	
947	−447.08	
		54.7
997	475.77	
		39.8
1047	1706.43	
	COS/B2[20]	
947	−931.64	
		55.0
997	3.6	
		37.8
1047	1297.0	
	COS/D	
947	−1112.8	
		46.2
997	1.3	
		37.2
1047	1318.0	

[a] Variables: ρ: density; p: pressure.

old models, which means that they all change their density ρ too much with changing temperature, while the COS/D model has a coefficient of thermal expansion α that is slightly too low.

The isothermal compressibility κ_T is listed in Table 7 for the same three water models. All models show results consistent with experiment.

Dynamic Properties. The dynamic properties of the models are listed in Table 8. The SPC water model shows a too large diffusion coefficient D, and the rotational relaxation times τ_l^{α}

TABLE 8: Dynamic Properties of the Different Water Models at 1 atm and 298.15 K (for expt, SPC, SPC/E, COS/D) and 300 K (for COS/B2, COS/G2)[a]

model	expt	SPC[59]	SPC/E[59]	COS/B2[20]	COS/G2[25]	COS/D
D/[10^{-9} m^2 s^{-1}]	2.3[77]	4.2	2.4	2.6	2.3	2.5
τ_2^{HH}/[ps]	2.0[78]	1.7	2.9	1.7	2.4	3.3
τ_2^{OH}/[ps]	1.95[79]	1.6	2.6	1.6	2.2	3.1
τ_2^{g}/[ps]	1.92[80]	1.4	2.5	1.6	2.0	3.0

[a] Variables: D: self-diffusion coefficient; τ_2^{α}: rotational relaxation times of different molecular axes.

TABLE 9: Dielectric Properties of the Different Water Models at 1 atm and 298.15 K (for expt, SPC, SPC/E, COS/D) and 300 K (for COS/B2, COS/G2)[a]

model	expt	SPC[59]	SPC/E[59]	COS/B2[20]	COS/G2[25]	COS/D
μ/[D]		2.27	2.35	2.62	2.59	2.43
μ^{ind}/[D]		0	0	0.58	0.78	0.56
$\varepsilon(0)$	78.4[81]	66.6	73.5	121.6	87.8	69.8
$\varepsilon(\infty)$	5.2,[81] 1.79[82]			2.67	3.18	2.37
τ_D/[ps]	8.3[81]	6.2	12.1	14.9	9.2	14.1
G_k		2.64	2.66	2.99		2.6
g_k	2.9[83]	2.51	2.61	3.55	2.53	2.51

[a] Variables: μ: average molecular dipole moment; μ^{ind}: average induced dipole moment per molecule; $\varepsilon(0)$: static dielectric permittivity; $\varepsilon(\infty)$: infinite frequency dielectric permittivity; τ_D: Debye dielectric relaxation time; G_k: finite system Kirkwood factor; g_k: infinite system Kirkwood factor.

are too short, which points to a too large mobility of this model. All polarizable models lower the value for the diffusion coefficient D. For the rotational relaxation times τ_l^{α}, the picture is not so clear. In the SPC/E, the COS/G2, and the COS/D models, the rotational relaxation is slower than that in experiment, while the COS/B2 has almost the same values as the SPC model.

Dielectric Properties. Table 9 displays the dielectric properties for the different water models. The dielectric permittivity $\varepsilon(0)$ is too low for the nonpolarizable models and too high for the polarizable ones, except for the damped COS model (COS/D). The dielectric permittivity $\varepsilon(0)$ is directly related to the average molecular dipole $\langle\mu\rangle$, as shown in Figure 2 and discussed by Guillot.[19] Guillot predicts a dipole moment of 2.4 D to reproduce the dielectric permittivity correctly, while Figure 2 suggests a value of 2.41 D. Experimentally, the value of the averaged dipole $\langle\mu\rangle$ in liquid water remains uncertain. The most recent experimental result suggests an average dipole moment $\langle\mu\rangle$ of water in the liquid phase of 2.9 $\pm$ 0.6 D,[30] while ab initio calculations predict a value between 2.33 and 3.0 D.[66−69]

The Debye dielectric relaxation time τ_D gives an approximation for the relaxation time of the hydrogen bond network. In contrast to the SPC model, the other models show larger Debye dielectric relaxation times τ_D than experiment. This overestimation is most probably due to the overestimation of the dielectric permittivity $\varepsilon(0)$ as they are related (see eq 14) and the lower mobility, as seen in Table 8.

Structure. The radial distribution functions (RDF) $g(r)$ for the O−O, O−H, and H−H distances are shown in Figure 3 for the COS/D model in comparison to the experimental data at 1 atm and 300 K. The overall shape of the radial distribution functions g_{OO} of the COS/D model is comparable to the one derived from experiment.[41] As in other polarizable models,[20] the first peak is overestimated, indicating a slightly overstructured liquid. The coordination numbers of 4.5 for the experiment and 4.3 for the COS/D model are obtained by integrating $g(r)$ to the first minimum in the curve (0.336 nm). The second and third peaks for the COS/D are slightly more pronounced than the curves derived from experimental data.

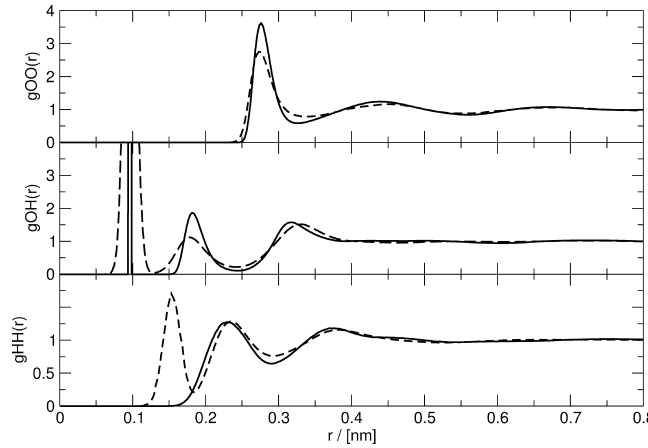

Figure 3. Liquid-phase radial distribution function at room temperature and pressure for the oxygen−oxygen pair (top), the oxygen−hydrogen pair (middle), and the hydrogen−hydrogen pair (bottom). The experimental results[41] are shown with a dashed line and the ones of the COS/D model with a solid line.

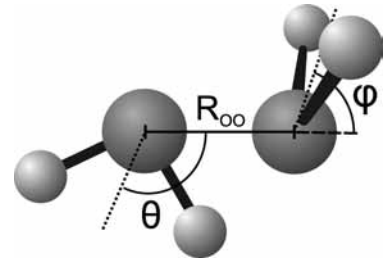

Figure 4. Definition of the water dimer geometry with the angles ϕ and θ and the distance R_{OO} that define the relative position and orientation of the monomers. Three atoms of the left monomer lie in one plane with the oxygen of the right monomer. The clockwise angle between the angular bisector of the left monomer and R_{OO} is θ. The vector between the hydrogen atoms of the other monomer is perpendicular to the mentioned plane. The counterclockwise angle ϕ is between the angular bisector of the right monomer and R_{OO}.

The g_{OH} curve shows the same type of agreement as the g_{OO} curve. The first peak is too pronounced and is shifted toward longer distances. The second peak has the correct height but is shifted toward shorter distances.

For the g_{HH} curve, the agreement with experimental data is good, with an only marginally shifted first peak.

3.2. Gas Phase. The dimer geometry as defined in Figure 4 was optimized for COS/D. It was calculated by performing a global conformational search in three dimensions (R_{OO}, θ, and ϕ) with the geometry of the monomers constrained to be rigid. The results are compared to the experimental findings in Table 10.

While all models give results close to the experimental one for the angle θ_{min}, the experimental angle ϕ_{min} is not properly reproduced by any of them. This less tetrahedral-like association of the monomers in the gas phase may lead to a deficiency in the description of the liquid structure, such as a wrong or missing density maximum. The wrong optimal dimer geometry also influences the μ^{dimer}, which strongly depends on the orientation of the molecules and is therefore not well reproduced by any of the described models for liquid water.

The dimer separation distance R_{OO}^{min} is underestimated by all water models compared to the experimental value. Here, the

TABLE 10: Gas-Phase Dimer Properties of Different Water Models[a]

model	expt	SPC[25]	SPC/E[25]	COS/B2[25]	COS/G2[25]	COS/D
R_{OO}^{min}/[nm]	0.297[84]	0.275	0.274	0.279	0.281	0.269
θ_{min}/[deg]	51[84]	52	52	51	56	58
ϕ_{min}/[deg]	57[84]	23	22	20	74	100
U_{pot}/[kJ mol^{-1}]	−22.7(2.5)[85]	−27.65	−30.10	−23.29	−20.90	−26.16
μ^{dimer}/[D]	2.6[84]	3.59	3.76	3.76	2.08	3.16
μ^{mean}/[D]		2.27	2.35	2.26	2.03	2.09

[a] The optimal (minimum-energy) geometry is defined by the O−O distance R(OO) and angles θ and ϕ as defined in Figure 4. Variables: U_{pot}: interaction energy; μ^{dimer}: total dipole moment; μ^{mean}: average molecular dipole moment.

TABLE 11: Properties of the COS/G2 and COS/D Models in the Solid State (ice I_h)[a]

Model	expt	COS/G2[25]	COS/D
ρ/[kg m^{-3}]	931.0[86]	958.0	946.7
μ/[D]	2.6,[87] 3.09[88]	2.81	2.53
μ_{ind}/[D]		0.97	0.67
U/[kJ mol^{-1}]	−47.34[89]	−49.05	−49.4

[a] Variables: ρ: density; μ: average molecular dipole moment; μ^{ind}: average induced dipole moment; U: lattice energy.

TABLE 12: Solvation Properties for an Argon Probe for Different Water Models at 300 K and 1 atm[a]

model	expt	SPC[55]	SPC/E[55]	COS/G2[2]	COS/D
ΔG_S/[kJ mol^{-1}]	8.4[90]	8.5	8.9	8.9	8.6
$-\Delta H_{uv}$/[kJ mol^{-1}]		10.2	10.5	12.0	12.1
$-T\Delta S_{uv}$/[kJ mol^{-1}]		18.7	19.4	20.9	20.7

[a] ΔG_S: solvation free enthalpy of a single argon molecule; ΔH_{uv}: argon solvation solute−solvent interaction enthalpy; ΔS_{uv}: argon solvation solute−solvent interaction entropy.

COS/B2 and COS/G2 models give some improvement compared to SPC and SPC/E, but the COS/D model shows an even smaller separation.

The binding strength that is overestimated by the nonpolarizable models SPC and SPC/E is better reproduced by the polarizable models COS/B2 and COS/G2. The damped polarizable model COS/D still gives a too strong binding strength which is, however, closer to the experimental one than that of the nonpolarizable models.

The difference in the potential energy between the optimized dimer structure and the ideal dimer structure is, however, only 2.9 kJ mol^{-1}, a difference that can easily be overcome in a simulation at room temperature.

3.3. Ice. To complete the investigation, the results for the I_h ice are shown in Table 11. The COS/G2 and the COS/D models give only a slightly too high density ρ. The dipole is lower for the COS/D model, as is expected as a direct result of the damping.

3.4. Hydrophobic Solvation. The results for the solvation of an argon probe in water are given in Table 12. The COS/D model does slightly better than COS/G2 and SPC/E. Compared to SPC, it shows a 20% larger compensation of the argon solvation solute−solvent interaction enthalpy ΔH_{uv}, and the entropic argon solvation solute−solvent interaction costs ΔS_{uv}. This leads to a slightly higher solvation free enthalpy ΔG_S. We note that the argon model was not parametrized using a COS/D type of polarizable model.

4. Conclusion

The presented polarizable water model is of the COS type, which avoids complex evaluation of the dipole−dipole interactions and forces as all electrostatic interactions are point charge interactions. The polarizable COS/D model has five interaction sites per molecule. Compared to the nonpolarizable SPC model with three interaction sites per molecule, the computational costs are approximatly a factor 5 higher. The introduced damping mimics the effect of hyperpolarizability in a scalar isotropic way.

The introduced damping of the polarizability α allows for a reduction of the dielectric permittivity $\varepsilon(0)$ of polarizable models to values significantly under the experimental value. It reduces the effect of overpolarization, but it influences other quantities. Especially the radial distribution function $g_{OO}(r)$, which was rather insensitive to a variation of parameters in previous parametrizations,[25,59] showed a visible response. Using a COS model with its virtual charge site at the oxygen position, it turned out to be impossible to simultaneously obtain the heat of vaporization ΔH_{vap}, the density ρ, the radial distribution function $g_{OO}(r)$, and the dielectric permittivity $\varepsilon(0)$ close to their experimental values. By using a virtual site that is different from the oxygen positon, a better model could be derived, the COS/D model.

The average dipole moment of the water molecules $\langle\mu\rangle$ turned out to be a fast computable first approximation for the slowly converging dielectric permittivity $\varepsilon(0)$. Yet, the targeted dielectric permittivity $\varepsilon(0)$ of 78.5 was not exactly reached for the COS/D model with a value of 69.8 and an average molecular dipole $\langle\mu\rangle$ of 2.43 D.

For the pure liquid, the inclusion of damped polarizability does not significantly improve the reproduction of thermodynamic properties. Yet, the developed COS/D model is expected to show more realistic behavior in simulations in which single water molecules are in different sites experiencing different electric field strengths, such as in proteins or within protein−protein or protein−DNA interfaces.

Acknowledgment. The authors thank Daan Geerke, Merijn Schenk, and Bruno Araujo Cautiero Horta for fruitful discussions. This work was financially supported by the National Center of Competence in Research (NCCR) in Structural Biology and by Grants 200021-109227 and 200020-121913 of the Swiss National Science Foundation, which are gratefully acknowledged.

References and Notes

(1) Oostenbrink, C.; Villa, A.; Mark, A. E.; van Gunsteren, W. F. *J. Comput. Chem.* **2004**, *25*, 1656–1676.
(2) Geerke, D. P.; van Gunsteren, W. F. *Mol. Phys.* **2007**, *105*, 1861–1881.
(3) Grossfield, A.; Ren, P. Y.; Ponder, J. W. *J. Am. Chem. Soc.* **2003**, *125*, 15671–15682.
(4) Maple, J. R.; Cao, Y. X.; Damm, W. G.; Halgren, T. A.; Kaminski, G. A.; Zhang, L. Y.; Friesner, R. A. *J. Chem. Theory Comput.* **2005**, *1*, 694–715.
(5) Chang, T. M.; Dang, L. X. *J. Phys. Chem. B* **2005**, *109*, 5759–5765.
(6) Patel, S. A.; Brooks, C. L. *J. Chem. Phys.* **2006**, *124*, 204706.

(7) Warshel, A.; Kato, M.; Pisliakov, A. V. *J. Chem. Theory Comput.* **2007**, *3*, 2034–2045.
(8) Xie, W. S.; Pu, J. Z.; MacKerell, A. D.; Gao, J. L. *J. Chem. Theory Comput.* **2007**, *3*, 1878–1889.
(9) Harder, E.; Anisimov, V. M.; Whitfield, T. W.; MacKerell, A. D.; Roux, B. *J. Phys. Chem. B* **2008**, *112*, 3509–3521.
(10) Rick, S. W.; Stuart, S. J. Potentials and algorithms for incorporating polarizability in computer simulations. In *Reviews in Computational Chemistry*; Wiley-VCH, Inc: New York, 2002; Vol 18, pp 89−146.
(11) Yu, H. B.; van Gunsteren, W. F. *Comput. Phys. Commun.* **2005**, *172*, 69–85.
(12) Warshel, A.; Levitt, M. *J. Mol. Biol.* **1976**, *103*, 227–249.
(13) Vesely, F. J. *J. Comput. Phys.* **1977**, *24*, 361–371.
(14) van Belle, D.; Couplet, I.; Prevost, M.; Wodak, S. J. *J. Mol. Biol.* **1987**, *198*, 721–735.
(15) Straatsma, T. P.; McCammon, J. A. *Mol. Simul.* **1990**, *5*, 181–192.
(16) Drude, P. *The Theory of Optics*; Longmans, Green, and Co.: New York, 1902.
(17) Born M.; Huang, K. *Dynamic Theory of Crystal Lattices*; Oxford University Press: Oxford, U.K., 1954.
(18) Rick, S. W.; Stuart, S. J.; Berne, B. J. *J. Chem. Phys.* **1994**, *101*, 6141–6156.
(19) Guillot, B. *J. Mol. Liq.* **2002**, *101*, 219–260.
(20) Yu, H. B.; Hansson, T.; van Gunsteren, W. F. *J. Chem. Phys.* **2003**, *118*, 221–234.
(21) Applequist, J.; Carl, J. R.; Fung, K. K. *J. Am. Chem. Soc.* **1972**, *94*, 2952–2960.
(22) Thole, B. T. *Chem. Phys.* **1981**, *59*, 341–350.
(23) Neufeld, E.; Yu, H.; Hansson, T.; van Gunsteren, W. *Polarizable water models and dielectric permittivity*; Technical Report; ETH: Zürich, Switzerland, 2003.
(24) Baranyai, A.; Bartok, A. *J. Chem. Phys.* **2007**, *126*, 184508.
(25) Yu, H. B.; van Gunsteren, W. F. *J. Chem. Phys.* **2004**, *121*, 9549–9564.
(26) Maroulis, G. *J. Chem. Phys.* **1991**, *94*, 1182–1190.
(27) Kaatz, P.; Donley, E. A.; Shelton, D. P. *J. Chem. Phys.* **1998**, *108*, 849–856.
(28) Maroulis, G. *Chem. Phys. Lett.* **1998**, *289*, 403–411.
(29) Svishchev, I. M.; Kusalik, P. G.; Wang, J.; Boyd, R. J. *J. Chem. Phys.* **1996**, *105*, 4742–4750.
(30) Badyal, Y. S.; Saboungi, M. L.; Price, D. L.; Shastri, S. D.; Haeffner, D. R.; Soper, A. K. *J. Chem. Phys.* **2000**, *112*, 9206–9208.
(31) Geerke, D. P.; van Gunsteren, W. F. *J. Chem. Theory Comput.* **2007**, *3*, 2128–2137.
(32) Kell, G. S. *J. Chem. Eng. Data* **1967**, *12*, 66–69.
(33) van Gunsteren, W. F.; Kruger, P.; Billeter, S. R.; Mark, A. E.; Eising, A. A.; Scott, W. R. P.; Hünenberger, P. H.; Tironi, I. G. *Biomolecular simulation: the GROMOS96 manual and user guide*; VDF: Zürich, Switzerland, 1996.
(34) Scott, W. R. P.; Hünenberger, P. H.; Tironi, I. G.; Mark, A. E.; Billeter, S. R.; Fennen, J.; Torda, A. E.; Huber, T.; Kruger, P.; van Gunsteren, W. F. *J. Phys. Chem. A* **1999**, *103*, 3596–3607.
(35) Ryckaert, J. P.; Ciccotti, G.; Berendsen, H. J. C. *J. Comput. Phys.* **1977**, *23*, 327–341.
(36) Berendsen, H. J. C.; Postma, J. P. M.; van Gunsteren, W. F.; Dinola, A.; Haak, J. R. *J. Chem. Phys.* **1984**, *81*, 3684–3690.
(37) Neumann, M. *J. Chem. Phys.* **1985**, *82*, 5663–5672.
(38) Tironi, I. G.; Sperb, R.; Smith, P. E.; van Gunsteren, W. F. *J. Chem. Phys.* **1995**, *102*, 5451–5459.
(39) Hayward, J. A.; Reimers, J. R. *J. Chem. Phys.* **1997**, *106*, 1518–1529.
(40) Postma, J. P. M. Ph.D. Thesis, Rijksuniversiteit, Groningen, The Netherlands, 1985.
(41) Soper, A. K. *Chem. Phys.* **2000**, *258*, 121–137.
(42) Berendsen, H. J. C. *Simulating the physical world*, 1st ed.; Cambridge University Press: Cambridge, U.K., 2007.
(43) Rothschild, W. G. *Dynamics of molecular liquids*; Wiley: New York, 1984.
(44) Berne, B. J.; Pecora, R. *Dynamic light scattering with applications to chemistry, biology, and physics*; Wiley: New York, 1976.
(45) Fleming, G. R. *Chemical applications of ultrafast spectroscopy*; Oxford University Press: New York, 1986.
(46) Neumann, M. *Mol. Phys.* **1983**, *50*, 841–858.
(47) van der Spoel, D.; van Maaren, P. J.; Berendsen, H. J. C. *J. Chem. Phys.* **1998**, *108*, 10220–10230.
(48) Neumann, M.; Steinhauser, O.; Pawley, G. S. *Mol. Phys.* **1984**, *52*, 97–113.
(49) Kindt, J. T.; Schmuttenmaer, C. A. *J. Phys. Chem.* **1996**, *100*, 10373–10379.
(50) Debye, P. J. W. *Polar molecules*; Chemical Catalog Company: New York, 1929.
(51) Tironi, I. G.; van Gunsteren, W. F. *Mol. Phys.* **1994**, *83*, 381–403.
(52) Motakabbir, K. A.; Berkowitz, M. *J. Phys. Chem.* **1990**, *94*, 8359–8362.
(53) Widom, B. *J. Chem. Phys.* **1963**, *39*, 2808.
(54) Schweke, D.; Haas, Y. *J. Phys. Chem. A* **2003**, *107*, 9554–9560.
(55) van der Vegt, N. F. A.; van Gunsteren, W. F. *J. Phys. Chem. B* **2004**, *108*, 1056–1064.
(56) Yu, H. A.; Karplus, M. *J. Chem. Phys.* **1988**, *89*, 2366–2379.
(57) Berendsen, H. J. C.; Postma, J. P. M.; van Gunsteren, W. F.; Hermans, J. *Interaction models for water in relation to protein hydration*; Intermolecular forces; Reidel: Dordrecht, The Netherlands, 1981.
(58) Berendsen, H. J. C.; Grigera, J. R.; Straatsma, T. P. *J. Phys. Chem.* **1987**, *91*, 6269–6271.
(59) Glattli, A.; Daura, X.; van Gunsteren, W. F. *J. Chem. Phys.* **2002**, *116*, 9811–9828.
(60) van Maaren, P. J.; van der Spoel, D. *J. Phys. Chem. B* **2001**, *105*, 2618–2626.
(61) Stern, H. A.; Rittner, F.; Berne, B. J.; Friesner, R. A. *J. Chem. Phys.* **2001**, *115*, 2237–2251.
(62) Lamoureux, G.; MacKerell, A. D.; Roux, B. *J. Chem. Phys.* **2003**, *119*, 5185–5197.
(63) Wu, Y. J.; Tepper, H. L.; Voth, G. A. *J. Chem. Phys.* **2006**, *124*, 024503.
(64) Lamoureux, G.; Harder, E.; Vorobyov, I. V.; Roux, B.; MacKerell, J., A. D. *Chem. Phys. Lett.* **2006**, *418*, 245–9.
(65) Chen, F.; Smith, P. E. *J. Chem. Phys.* **2007**, *126*, 221101.
(66) Morita, A.; Kato, S. *J. Chem. Phys.* **1999**, *110*, 11987–11998.
(67) Delle Site, L.; Alavi, A.; Lynden-Bell, R. M. *Mol. Phys.* **1999**, *96*, 1683–1693.
(68) Silvestrelli, P. L.; Parrinello, M. *J. Chem. Phys.* **1999**, *111*, 3572–3580.
(69) Dyer, P. J.; Cummings, P. T. *J. Chem. Phys.* **2006**, *125*, 144519.
(70) Hasted, J. *Liquid water: Dielectric properties; Water, A Comprehensive Treatise*; Plenum Press: New York, 1972.
(71) Ichikawa, K.; Kameda, Y.; Yamaguchi, T.; Wakita, H.; Misawa, M. *Mol. Phys.* **1991**, *73*, 79–86.
(72) Shostak, S. L.; Ebenstein, W. L.; Muenter, J. S. *J. Chem. Phys.* **1991**, *94*, 5875–5882.
(73) Russell, A. J.; Spackman, M. A. *Mol. Phys.* **1995**, *84*, 1239–1255.
(74) Bishop, D. M.; Cheung, L. M. *J. Phys. Chem. Ref. Data* **1982**, *11*, 119–133.
(75) Geerke, D. P.; van Gunsteren, W. F. *J. Phys. Chem. B* **2007**, *111*, 6425–6436.
(76) Weast, R. C. *Handbook of chemistry and physics*, 61st ed.; CRC Press: Boca Raton, FL, 1980.
(77) Krynicki, K.; Green, C. D.; Sawyer, D. W. *Faraday Discuss. Chem. Soc.* **1978**, 199–208.
(78) Halle, B.; Wennerstrom, H. *J. Chem. Phys.* **1981**, *75*, 1928–1943.
(79) Ludwig, R. *Chem. Phys.* **1995**, *195*, 329–337.
(80) Krynicki, K. *Physica* **1966**, *32*, 167–178.
(81) Lide, D. R. *Handbook of chemistry and physics*, 88th ed.; CRC Press/Taylor and Francis: Boca Raton, FL, 2007−2008.
(82) Buckingham, A. D. *Proc. R. Soc. London, Ser. A* **1956**, *238*, 235–244.
(83) Neumann, M. *Mol. Phys.* **1986**, *57*, 97–121.
(84) Odutola, J. A.; Dyke, T. R. *J. Chem. Phys.* **1980**, *72*, 5062–5070.
(85) Curtiss, L. A.; Frurip, D. J.; Blander, M. *J. Chem. Phys.* **1979**, *71*, 2703–2711.
(86) Rottger, K.; Endriss, A.; Ihringer, J.; Doyle, S.; Kuhs, W. F. *Acta Crystallogr., Sect. B* **1994**, *50*, 644–648.
(87) Coulson, C. A.; Eisenberg, D. *Proc. R. Soc. London, Ser. A* **1966**, *291*, 445–453.
(88) Batista, E. R.; Xantheas, S. S.; Jonsson, H. *J. Chem. Phys.* **1998**, *109*, 4546–4551.
(89) Whalley, E. *J. Chem. Phys.* **1984**, *81*, 4087–4092.
(90) Ben-Naim, A.; Marcus, Y. *J. Chem. Phys.* **1984**, *81*, 2016–2027.

JP903164S